# Characterization of Nucleation of Methane Hydrate Crystals: Interfacial Theory and Molecular Simulation

*Sina Mirzaeifard, Phillip Servio, Alejandro D. Rey**

Department of Chemical Engineering, McGill University, Montreal H3A 0C5, Canada

**Abstract:**

*Hypothesis:*

Solutions of water and methane gas at favorable thermodynamic conditions lead to the formation of crystalline methane hydrates. In natural and industrial environments, the nucleation process might occur in the solution's bulk or at the solid-liquid and liquid-gas interfaces, which evolve into distinct morphologies. A complete molecular level understanding and material characterization of preferred nucleation sites and morphologies is required to inhibit or promote crystallization, as required.

*Methodology:*

Computational simulations are utilized in this work in combination with analytical theory to calculate the supersaturation and interfacial tension as the driving force and suppressor, respectively, in the hydrate crystal formation process. We employ accurate molecular dynamics (MD) techniques to obtain critical thermodynamic and mechanical properties, and subsequently, analyze the formation using the classical nucleation theory (CNT).

*Findings:*

We report the interfacial tension at all possible interfaces in water-methane gas solutions. We apply both our direct numerical simulation method and Antonow's rule to find the tension at the methane

hydrate and gas interface, and importantly conclude that Antonow's rule overestimates the values. We calculate the work of formation and nucleation rate of the methane hydrate with and without additives. The nucleation probabilistically forms in the ranked order of film-shaped, cap-shaped, lens-shaped, and homogeneous. We postulate that the premelting of hydrate crystals at the hydrate-gas interface creates an intermediate quasi-liquid layer, which works in favor of the lens-shaped formation compared to homogeneous cases. However, the subtle difference in surface energy indicates high concentration of water and gas molecules at the interface is the main reason behind lens-shaped clustering. We lastly show that ice properties cannot be used to approximate the hydrate formation work.

**Keywords:** Methane hydrate; Surface physics; Interfacial tension; Classical nucleation theory; Computational thermodynamics; Molecular dynamics simulation.

## Introduction

At low temperature and high pressure, liquid water molecules form hydrogen bonded networks that create polyhedral cages, which can encapsulate guest gas molecules such as methane, ethane, and propane so that a new phase of ice-like crystals forms above 0 ºC, known as gas hydrate or clathrate [1]. Depending on the guest gas molecules, the hydrates can form different crystalline structures including structure I [2], structure II [3, 4], and structure H [5]. Gas hydrates have a wide range of industrial applications. They play a very important role in flow assurance (i.e., management of fluid transportation in multiphase flow) as the pipelines are mostly in deep oceans that provide favorable thermodynamic conditions for gas hydrates formation, which consequently causes explosions or blockage inside the pipelines and equipment [6, 7]. The blockage can be extremely costly as it is usually followed by a shutdown in the entire oil and gas processing plants that might take days or weeks to be resolved. Unfortunately, the current techniques that are being used to avoid the blockage are also environmentally damaging. In addition to flow assurance, hydrates can be considered a vastly available clean resource of energy, and also transportation medium for other materials as one volume of gas hydrate contains 164 volumes of gas at standard

temperature and pressure condition [1]. Moreover, self-preservation is a unique and poorly understood characteristic of gas hydrates that increases and prolongs its stability, which is desirable for gas storage applications [8].

Methane hydrates are the most common hydrates formed naturally by biogenic methane in marine and under permafrost sediments. These naturally occurring hydrates hold two to three orders of magnitude the amount of energy when compared to global fossil fuels and natural gas reserves, respectively [6-11]. On the other hand, the ubiquitous methane hydrate could be a significant contributor to global warming if methane is released and migrates to the ocean's surfaces. Hence, the significance of methane hydrates in environmental processes has been subjected to intense research [9]. In summary, we seek to understand the methane hydrate formation process in order to eventually find green and robust methods to inhibit or promote these clathrates, depending on the application.

The fundamental thermodynamic conditions to ignite the formation process are high pressure (> 0.6 MPa), low temperature (< 323 K), the presence of guest molecules as the hydrate former, and sufficient amount of water [8, 12]. Additional conditions such as turbulence or agitation, presence of nucleation sites, and free water might enhance the formation rate [5]. Due to the availability of all these essential parameters in some environments like gas pipelines, the formation probability is substantial. This formation phenomenon includes nucleation and growth processes as the onset of hydrate plugging in flow assurance that has been studied for years, however, there is so much yet to comprehend [13-15].

The thermodynamic temperature and pressure condition for hydrate formation must be in the region of hydrate stability. In general, for a pair of solute-solvent, there exists a relationship for concentration and temperature that defines the metastable limit. This relationship is known as the thermodynamic spinodal and represents the supersaturation limit. However, the formation of metastable hydrates is challenged due to high entropy conditions until the cluster agglomerate reaches a critical crystal nuclei for steady growth [1]. Supersaturated systems can create a new phase either in the bulk (homogenous) or onto the surface in contact with the bulk (heterogeneous). Depending on the location of the contact interface, heterogeneous nucleation can be further categorized into three models: lens-shaped (gas-liquid), film-shaped (gas-liquid), and cap-shaped (solid-liquid). Figure 1 shows a schematic diagram of these formation mechanisms.

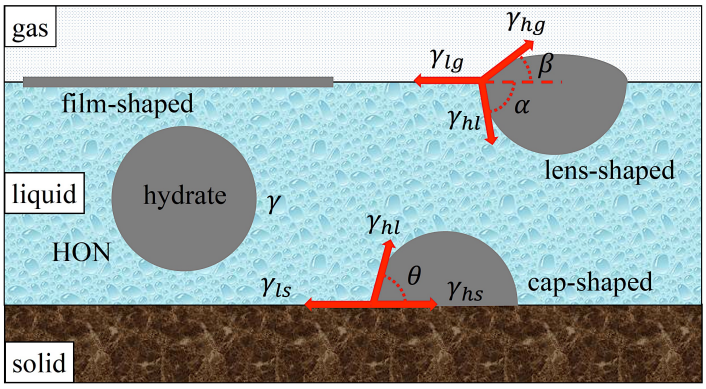


**Figure 1.** Schematics of different hydrate formation morphologies. $\gamma$ represents the interfacial tension for the homogeneous (HON) formation of methane gas hydrate. $\gamma_{lg}$, $\gamma_{hl}$, $\gamma_{hg}$, $\gamma_{ls}$, and $\gamma_{hs}$ indicate the interfacial tension at the liquid-gas, hydrate-liquid, hydrate-gas, liquid-solid, and hydrate-solid interfaces, respectively.

Among all the theories in crystallography, the classical nucleation theory (CNT) is still the foundation of most state-of-the-art nucleation models, which fruitfully describes the gas hydrate or ice formation work [1, 16-18]. According to the CNT, this work equals a spontaneous formation of a new hydrate cluster consisting of *n* crystal unit cells associated with an interfacial energy cost [19]. This formation work $W(n)$ is given by:

$$W(n) = -n\Delta\mu + c(nv_h)^{\frac{2}{3}}\gamma \quad (1)$$

where $\Delta\mu$ (J) measures the supersaturation (i.e., difference in chemical potentials) as a function of pressure and temperature, $c$ is a shape factor, $v_h$ ($m^3$) is the volume of a hydrate building unit, and $\gamma$ ($J/m^2$) accounts for the interfacial energy.

**Motivation**

It has been assumed that the interfacial boundaries between different phases dictate the ideal mechanism and location for clathrate formation [19, 20], but the accuracy of this assumption needs to be critically examined. It is known that the formation of hydrate crystals, irrespective of the hydrate promoters and system pressure [21], mainly depends on the nucleation period, which is

influenced by the driving forces and interfacial energy [20, 22, 23], but the molecular-level understanding of these contributions remains incomplete.

In particular, the characterization of interfacial tensions at water-methane hydrate, water-methane gas, and methane hydrate-methane gas interfaces in the range of 271-289 K and 5-15 MPa, which is the methane hydrate stability and formation region [11], is essentially missing or very limited. More specifically, to obtain the interfacial tension between methane gas and liquid phases, the Antonow's (Antonoff's) rule has been proposed [19], while the reliability of such classical thermodynamic relation in complex crystalline hydrate surfaces is very uncertain. This substantial lack of information on the interfacial tension, as well as supersaturation data, generate significant questions in our understanding of hydrate formation process: is it homogeneous [24-26], cap-shaped [27-30], or lens-shaped [30, 31]. In the case of lens-shaped morphology, it is also unclear what causes this type of formation. This can be due to the role of interface in the Gibbs free energy of nucleation or simply higher concentrations of both water and methane molecules at the water-gas interface. Nonetheless, the water mole fraction in bulk gas and gas mole fraction in aqueous phase are less than 0.05 and 0.001, respectively [1], which impedes the homogeneous formation, however, previous works reported the possibility of such formation process [25, 32-35].

In the case of full occupancy of hydrate cages, 85 mol% of the crystal hydrate is still made of water molecules [12], which may result in similar physical and thermodynamic behaviors for ice and methane hydrate. Therefore, some researchers suggested the use the properties of ice properties to eliminate the need of critically important hydrate data [19, 36, 37]. Despite many ice-hydrate analogies, some properties such as mechanical strength, heat capacity, and thermal conductivity are different [6-8]. Therefore, we need to investigate the possibility of using ice parameters in hydrate formation studies to ensure accurate results and conclusions.

Hence, the leading motivation of this work is to characterize the supersaturation and interfacial energy contributions in the nucleation process of methane gas hydrates, and subsequently, reveal the theoretical physics behind the most probable formation process in order to promote or suppress it subject to the above-mentioned technological applications. To the best of our knowledge, this is the first work that attempts to simultaneously study the water-gas, water-hydrate, and hydrate-gas mixtures to answer all these crucial questions in hydrate science. Furthermore, based on the

interfacial characterization, we deduce features of the homogeneous and heterogeneous nucleation of methane hydrates.

The organization of this paper is as follows. In the next section, we briefly describe the computational methodology and models, MD computer simulations, and analytical theory, which include a novel approach for the calculation of supersaturation and interfacial tension at the liquid-gas, hydrate-liquid, and hydrate-gas interfaces. In the results and discussion section, we calculate and analyze the interfacial tension, supersaturation, hydrate formation work, and crystal nucleation rate at different pressure and temperature. In addition, we investigate the effect of additives in the water-methane solution. We also evaluate substituting hydrate parameters with ice when the interfacial tension is unknown. Lastly, we articulate the main conclusions, significance, and novelty of this work.

**Methodology**

The nature of interfacial interactions and thermodynamic stability is of great significance to investigate the phase transitions, nucleation, morphology, and nucleation rate of gas hydrates, which demands modern experimental methods, theoretical modeling, or computational characterization [20, 38-42].

Clathrate hydrate formation is a nanoscale, rapid, and stochastic process, while the performed experiments cannot resolve these key characteristics [13]. In addition, the experimental characterization may be inaccurate owing to the sample impurities and absence of necessary molecular-level measurements, and furthermore, it is relatively complex and expensive to provide the crucial thermodynamic conditions (high pressure and low temperature), specifically in cases of the predominant natural gas hydrates in pipelines [43, 44]. Some of the current theoretical work has also not fully explained the hydrate formation owing to assumptions that will be explained later in this paper. In this work, we show that a combination of analytical theory and computational simulations can elucidate the thermodynamic and kinetic aspects of hydrate formation in both microscopic and macroscopic scales. Therefore, we attempt to accurately model clathrate hydrates to find more insights regarding the supersaturation and interfacial energy contributions in nucleation and growth processes. We use molecular dynamic (MD) techniques in conjunction with

interfacial thermodynamics to quantitatively and qualitatively explore the formation work, nucleation rate, and equilibrium configurations. Nevertheless, molecular simulations of different mixtures including liquid, gas, and solid crystals encounter challenges of its own to obtain reliable results. For instance, robust hydrogen and ion bonding, discontinuity of macroscopic fields, sudden local density variation, interfacial elastic deformation, topological disturbance, spontaneous interfacial expansion or contraction, and sufficient length and time scales. The key aspect of our approach is to employ appropriate methods to overcome these issues by tailoring realistic models [45, 46].

**Model**

In this study, we follow the standard procedure to create the different possible mixtures of interest: water-gas, water-hydrate, and hydrate-gas [47, 48]. In a 48×48×200 Å three-dimensional simulation box with periodic boundary conditions, we surround one phase with another phase at each side in order to construct three distinct interfaces of the water-methane hydrate, water-methane gas, and methane hydrate-methane gas (see Figure 2). Table 1 reports the number of molecules located in the initial configuration for each set of the simulations. Please note that the hydrate crystal phase contains water and methane molecules with 100% cage occupancy. We adopt initial Cartesian coordinates of the methane hydrate unit cell at the lowest energy configuration and zero dipole moment based on the X-ray diffraction analysis [49] and high-resolution neutron diffraction experiments [50].

We choose such phase-by-phase breakdown as an alternative to the regular three-phase system [51] to ensure more accurate results of the interfacial tension. This approach is of great importance for the hydrate surfaces since the interfacial elastic deformation differentiates the surface free energy and surface tension [52, 53], which demands distinct simulation and computation methods, not applied for liquid-gas interfaces. Moreover, this method creates two interfaces between each couple of phases, which allows us to average over two values obtained from both interfaces to increase the accuracy. Please note that the choice of pressure and temperature in this study is based on a region of phase diagram so that all three phases can coexist to guarantee equilibrium states for all the binary mixtures [1, 11].

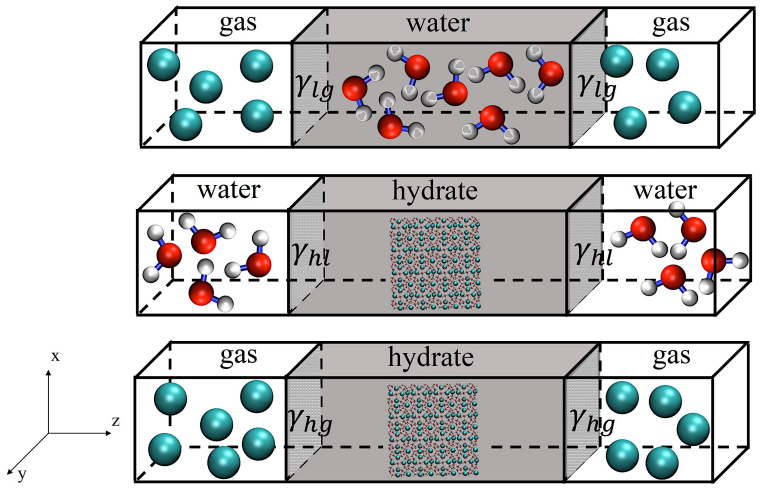


**Figure 2.** Schematic showing the simulations template including the methane gas, water, and methane hydrate molecules to represent the gas, liquid, and hydrate phases, respectively. The red, white, and green particles denote the oxygen and hydrogen atoms, and methane molecules, respectively.

**Table 1.** Number of molecules for the initial configuration

| mixtures | phases | | | |
|---|---|---|---|---|
| | gas | liquid | hydrate | |
| gas-water | 1,328 $CH_4$ | 13,104 $H_2O$ | - | |
| water-hydrate | - | 5,468 $H_2O$ | 1,328 $CH_4$ | 7,636 $H_2O$ |
| gas-hydrate | 660 $CH_4$ | - | 1,016 $CH_4$ | 5,842 $H_2O$ |

In this work, we use the united atom optimized potentials for liquid simulations (OPLS-UA) [54] and transferable intermolecular potential with the four points (TIP4P) models [55] to create force fields for the methane and water molecules, respectively, employing the LAMMPS software [56]. We choose TIP4P as opposed to other water models, such as SPC/E, TIP3P, and TIP5P, which is more compatible with mixtures of water and hydrophobic solutes [57-59]. To include the Coulombic electrostatic interactions, we execute the TIP4P-optimized particle-particle particle-

mesh (PPPM) package with an accuracy of $10^{-5}$ for the force computation following the introduced approach by Hockney and Eastwood [60, 61]. In addition, the Lennard-Jones (LJ) potential with Lorentz-Berthelot mixing rule is used to implement the intermolecular interactions:

$$U_{LJ}(r) = 4\varepsilon\left[\left(\frac{\sigma}{r}\right)^{12} - \left(\frac{\sigma}{r}\right)^{6}\right] \quad (2)$$

$$\varepsilon_{ij} = \sqrt{\varepsilon_{ii}\varepsilon_{jj}}\ ,\ \sigma_{ij} = \frac{\sigma_{ii}+\sigma_{jj}}{2} \quad (3)$$

where $\varepsilon$, $\sigma$, and r denote the well depth, finite distance at zero potential, and particles distance, respectively, as reported in Table 2 [54, 55]. We choose a cut-off distance of 12 Å for both Coulombic electrostatic and LJ interactions. We also constrain the bond lengths and angles integrated in the water molecules by means of the Shake algorithm to avoid any substantial variation throughout the simulations.

**Table 2.** Simulation parameters including the molecular and structural properties of the water and methane molecules

| | mass (g/mol) | $\sigma$ (Å) | $\varepsilon$ (kcal/mol) | charge (e) |
|---|---|---|---|---|
| $CH_4$ | 16.042 | 3.733 | 0.294 | 0 |
| O | 15.999 | 3.164 | 0.163 | -1.0484 |
| H | 1.0080 | 0 | 0 | 0.5242 |
| H-O-H angle | | 104.52° | | |
| O-H bond length | | 0.9572 Å | | |
| O···M distance | | 0.125 Å | | |

**Simulation**

We apply the Verlet algorithm with a time step of 2 fs to incorporate the non-Hamiltonian equations of motion. Accordingly, Nosé-Hoover thermostat and Parrinello-Rahman barostat adjust the pressure and temperature with 4 ps damping constant for the characteristic fluctuations. We

sample the system configurations using the isothermal-isobaric (*NPT*) and isothermal-isobaric-isointerface area ($NP_NAT$) ensembles. The novel and effective $NP_NAT$ ensemble, which requires constant normal pressure ($P_N$) and cross-sectional area ($A$) can precisely capture interfacial phenomena under different temperature and pressure regimes. The $NP_NAT$ ensemble controls the normal pressure in the z direction ($P_{ZZ}$) by the barostat. The system volume, and subsequently, the densities of coexisting-components can change towards equilibration to attain a desired target pressure. The ensemble also holds constant the surface area by fixing the simulation box length in both x ($L_x$) and y ($L_y$) directions (i.e., $A_S = L_xL_y$) with independent contraction or dilation in only the z dimension. The box length in the z direction ($L_z$) freely fluctuates to adjust the system volume for the prescribed bulk density of each phase so that the knowledge on the initial value of $L_z$ is not necessary

We start the simulations with an initial configuration, and run for 300 ns under the standard *NPT* ensemble to attain equilibrium and appropriate lattice parameters for cases with a hydrate phase. We continue to perform the MD simulations for further 10 ns until the thermodynamic equilibrium is guaranteed by the correlation factor calculations on thermodynamic and mechanical properties, namely, potential energy, temperature, and local densities of water and methane molecules. Thenceforth, we interchangeably employ the adaptive $NP_NAT$ and *NPT* ensembles throughout the simulations following the method fully descried in our previous work [62] to collect the required data throughout 5 ns of MD simulation. We only analyze and report the information obtained from the last nanosecond to ensure the most accurate results.

**Analytical Theory**

According to Eqn. (1), any analysis on the formation work demands the calculation of the supersaturation and interfacial tension contributions. Supersaturation of an isothermal and isobaric regimes is calculated from the following equation [19]:

$$\Delta\mu_{isothermal} = k_B T \, ln\left[\frac{\varphi(P,T)P}{\varphi(P_e,T)P_e}\right] + (n_w v_w - v_h)(P - P_e) \quad (4)$$

where $k_B$, T, $n_w$, $v_w$, P, and $P_e$ are Boltzmann constant, the system temperature, the stoichiometric hydration number defined as the ratio of the number of water to gas molecules (5.75, for methane hydrate [19]), which is a function of formation condition [9], the volume of water molecules in the solution (≈ 0.03 $nm^3$ [19]), the system pressure, and the equilibrium pressure, respectively. Please

note that we choose pressure and temperature close to their equilibrium values and Peng-Robinson equation of state to obtain the fugacity coefficient ($\varphi$) [63].

We employ the standard mechanical definition devised by Bakker *et al*. [64, 65] to compute the interfacial tension ($\gamma_B$). In addition, a method for the tail or long range correction developed by Blokhuis *et al*. [66] is included to compensate the truncation error triggered by applying a cut-off distance in the interatomic interactions [66-68]. In cases involving the crystalline hydrate phase, implementation of the Shuttleworth equation is also required to account for the elastic deformation of the solid surface [52, 69]. To account for this deformation requires the sequential use of the *NPT* and $NP_NAT$ ensembles to attain sensible results as completely described in our preceding work [62]. The total interfacial tension is given by:

$$\gamma = \overbrace{\frac{1}{2}\int_{-\infty}^{+\infty}\left(P_{zz} - \left(\frac{P_{xx}+P_{yy}}{2}\right)\right)dz}^{\gamma_B} + \overbrace{\int_0^1\int_{r_c}^{\infty} 12\pi\varepsilon\sigma^6{\Delta\rho_{ij}}^2\left(\frac{3s^3-s}{r^3}\right)cot\left(\frac{rs}{t}\right)dsdr}^{\gamma_{tail}}$$

$$+\overbrace{A_s\frac{\partial(\gamma_B+\gamma_{tail})}{\partial A_s}}^{\gamma_e} \quad (5)$$

where $P_{zz}$ and $\left(P_{xx}+P_{yy}\right)/2$, $r_c$, $t$, $s$, $\Delta\rho_{ij}$, and $A_S$ represent the normal pressure, tangential pressure, cut-off distance, interfacial thickness, position, molecular density difference between the i and j phases, and the cross-sectional area, respectively.

It should be noted that $\gamma$ is equal to the surface energy of methane hydrate-liquid interface ($\gamma_{hl}$) for the case of homogenous nucleation as shown in Figure 1. $\gamma$ for heterogeneous nucleation (HEN), which might occur at the interface of liquid-solid (cap-shaped) or liquid-gas (lens-shaped), is lower than $\gamma_{hl}$ obeying the following relationship [19]:

$$\gamma = \Psi\gamma_{hl} \quad (6)$$

where $\Psi$ is in a range of 0 to 1 to characterize different shapes of heterogeneous nucleation. For cap-shaped clusters, $\Psi$ can be calculated from [19]:

$$\Psi_{cap-shaped} = \left[\frac{(2+\cos\theta)(1-\cos\theta)^2}{4}\right]^{\frac{1}{3}} \quad (7)$$

where $\theta$ is called the wetting angle of hydrate-solid interface. This angle can range from 0 (complete wetting) to 180° (no wetting, which is HON). The Young equation relates $\theta$ to the surface energies of the liquid-solid ($\gamma_{ls}$) and hydrate-solid ($\gamma_{hs}$) interfaces by the following equation [37]:

$$\cos\theta = \frac{(\gamma_{ls}-\gamma_{hs})}{\gamma_{hl}} \quad (8)$$

Since the interaction with a solid substrate is not the scope of this work, we simply assign two candidates for the $\theta$: 60° as an acute angle and 120° as an obtuse angle. Figure 3 shows how the wetting angle alters the interfacial energy contribution via the parameter $\Psi$.

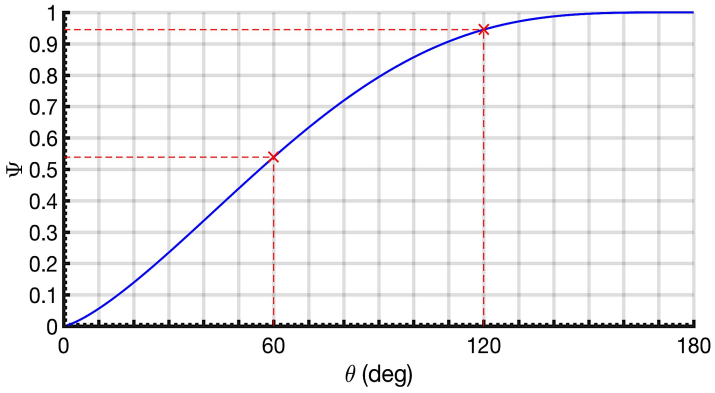


**Figure 3.** Characterization factor versus wetting angle with values between 0 to 180° for cap-shaped clusters.

For lens-shaped clusters, $\Psi$ is [19]:

$$\Psi_{lens-shaped} = \left[\frac{(2+\cos\alpha)(1-\cos\alpha)^2+(2+\cos\beta)(1-\cos\beta)^2\left(\frac{\sin\alpha}{\sin\beta}\right)^3}{4}\right]^{\frac{1}{3}} \quad (9)$$

similarly, $\alpha$ and $\beta$ are related to the surface energies of the liquid-gas ($\gamma_{lg}$) and hydrate-gas ($\gamma_{hg}$) interfaces by the following expressions [19]:

$$\cos\alpha = \frac{\left(\gamma_{lg}^2+\gamma_{hl}{}^2-\gamma_{hg}^2\right)}{2\gamma_{lg}\gamma_{hl}}, \cos\beta = \frac{\left(\gamma_{lg}^2-\gamma_{hl}{}^2+\gamma_{hg}^2\right)}{2\gamma_{lg}\gamma_{hg}} \quad (10)$$

According to Eqn. (9), $\Psi_{lens-shaped}$ is zero when α and β are infinitesimal, which eliminates the interfacial energy contribution from Eqn. (1). Such scenario effectively reveals the limit of lens-shaped formation denoted as film-shaped nucleation to seek insights when only spontaneous nucleation occurs in order to highlight the role of interfacial energy in hydrate formation work. Please note that the direct assignment of α and β is not necessary. These angles are intrinsically used to estimate the $\Psi_{lens-shaped}$ by the values of surface energy. Whenever possible, we validate the reliability of these methods and estimations with available experimental and computational data.

**Results and Discussion**

First, we calculate the interfacial tension for the liquid-gas and hydrate-liquid contact interfaces. We present all the details for the calculation methods of these two mixtures in our previous work [62, 70, 71]. We may obtain the interfacial energy associated with the interface between the methane gas and hydrate phases following a direct computation as explained earlier ($\gamma_{hg}$) or using the well-known Antonow's rule ($\gamma_{hg}^*$) proposed by Kashchiev *et al*. owing to the lack of data on the interfacial tension [19, 72, 73]:

$$\gamma_{hg}^* = \gamma_{hl} + \gamma_{lg} \quad (11)$$

Figure 4 reports the values of the interfacial tension between all the involved phases as required for the work calculation of methane hydrate formation. To evaluate the results, we compare them with the scarce existing studies on the water-methane hydrate and water-methane gas interfacial tensions in the pressure and temperature of interest (see Table 3). This work demonstrates a great agreement with an average deviation of 1.49%. The hydrate-liquid interfacial tension in this work also compares well with the interfacial tension of cyclopentane hydrate-liquid hydrocarbon and $CH_4/C_2H_6$ hydrate-liquid hydrocarbon mixtures, which are 47±5 mN/m [20, 74] and 53.3±0.5 mN/m [75], respectively. The interfacial tension at the liquid-gas interface decreases with temperature from 271 K to 289 K, while this temperature increase triggers a slight tension increase at the hydrate-liquid interface (see Figure 4a). However, the temperature does not seem to affect

the interfacial tension at the hydrate-gas interface. On the other hand, the interfacial tension at all the interfaces monotonically decreases with pressure from 5 MPa to 15 MPa (see Figure 4b).

**Table 3.** The available interfacial tension at the water-methane gas and methane hydrate-water interfaces

| Investigators | Year | P (MPa) | T (K) | $\gamma_{lg}$ (mN/m) | $\gamma_{hl}$ (mN/m) |
|---|---|---|---|---|---|
| Naeiji *et al*. [76] | 2017 | 6 | 275 | 67.3 | 39.3 |
| | | 10 | | 64.7 | 33.4 |
| | | 15 | | 60.8 | 31.7 |
| Kvamme *et al*. [77] | 2011 | 6 | 275 | 68.7 | |
| | | 10 | | 62.7 | |
| Schmidt *et al*. [78] | 2003 | 5 | 275 | 69.9 | |
| | | 6 | | 68.5 | |
| | | 7 | | 65.5 | |
| | | 8 | | 63.9 | |
| | | 9 | | 62.7 | |
| | | 10 | | 61.5 | |
| Jho *et al*. [79] | 2002 | 5 | 275 | 68.1 | |
| | | 6 | | 66.0 | |
| | | 7 | | 64.6 | |
| | | 8 | | 63.3 | |
| | | 9 | | 62.1 | |
| | | 10 | | 60.0 | |

| | | | | |
|---|---|---|---|---|
| Jacobson *et al*. [80] | 2011 | 6 | 275 | 36±2 |
| Anderson *et al*. [81] | 2003 | 10 | 275 | 32±3 |
| Uchida *et al*. [82] | 2002 | 10 | 275 | 34±6 |

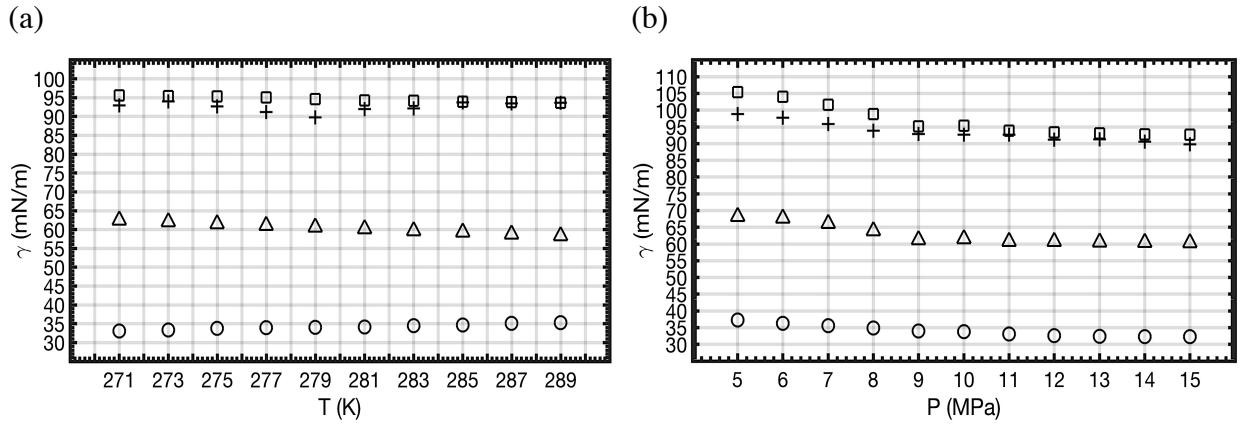


**Figure 4.** The interfacial tension at different temperature (a) and pressure (b). The triangle, circle, plus sign, and square markers represent $\gamma_{lg}$, $\gamma_{hl}$, $\gamma_{hg}$, and $\gamma_{hg}^{*}$.

However, the two calculation methods of interfacial tension between the methane hydrate and gas phases reveal the same trends with temperature and pressure in analogous manner to the ice-air interfacial tension [83-85], the direct approach seems to continuously provide lower values at different pressure and temperature. To guarantee the most reliable results for formation work, we need to find the reason behind the deviation, and subsequently, select the correct values for the subsequent calculations.

Figure 5 shows a snapshot of the methane gas and hydrate mixture at 275 K and 10 MPa. We visually observe a narrow liquid-like phase of water molecules between the crystalline hydrate and gas molecules originated from the premelting of the hydrate molecules at its surface [86, 87]. The existence of such intermediate quasi-liquid layer has been reported for both ice [88-90] and hydrates [91] mixtures, which explains the function of the Antonow's rule by some means. Herein, we postulate this thin layer presence may relate to the discussed deviation between the two calculation routes of hydrate-gas interfacial tension.

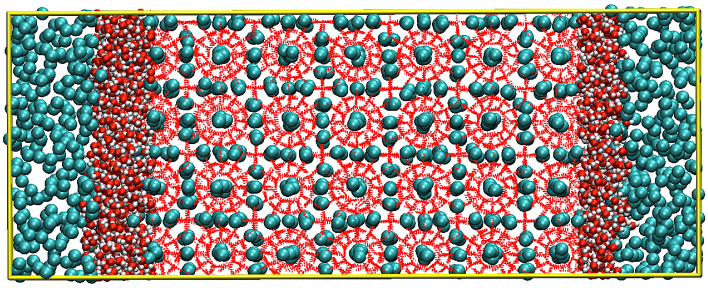

**Figure 5.** Snapshot of a mixture configuration composed of methane hydrate and gas phases. The green, red, and white particles represent the methane molecules, oxygen atoms, and hydrogen atoms, respectively. The red lines denote the hydrogen bonding between the water molecules forming the structure I methane hydrate. The transitional liquid-like phase can be readily distinguished at the methane hydrate-gas interface.

Hence, we evaluate the attractive and repulsive interactions between the methane gas and hydrate boundary surfaces through a series of calculations on the disjoining pressure (Π) [92, 93] to obtain the film spreading coefficient ($S$) [94, 95], which measures the spontaneous spreading of the quasi-liquid layer:

$$\Pi = P_{QL} - P_{\infty} \tag{12}$$

$$S = \int_{\delta_{QL}}^{\infty} \Pi \mathrm{d}\delta_{QL} \tag{13}$$

where $P_{QL}$, $P_{\infty}$, and $\delta_{QL}$ represent the internal pressure in the transitional quasi-liquid layer, the bulk pressure, and the quasi-liquid layer thickness, respectively. Therefore, we require the quasi-liquid layer thickness in a range of pressures and temperatures. We systematically increase the system temperature from 271 K up to 295 K to find the temperature, at which hydrate dissociation continues to a full melting process. Hence, we establish the melting temperature ($T_m$) at 289 K to measure the subcooling (i.e., $\Delta T_m = T_m - T$). We measure the intermediate liquid-like layer thickness from the charge and local density fluctuations across the interface (see Figure 6a). Since the water, methane, and hydrate molecules can be distinguished by their density and charge

quantities, we use these criteria to determine the boundaries of this layer. For instance, as we move from the methane gas to hydrate phase in the z-direction, the local molecular densities of water and methane gas at 275 K and 10 MPa simultaneously shift from approximately 0 and 0.16 g/cm$^3$ to near 1 and 0 g/cm$^3$, respectively, which represent the boundary of liquid-like layer. Thereafter, the density undulation of crystalline hydrate structure identifies the other boundary of this layer. The charge distribution also follows the density variations and moves from a nonpolar methane gas phase to polar liquid phase. Figure 6b shows such thickness decreases with pressure, while it increases with rising temperature (lower subcooling). Please note that this thickness decrease is limited in any temperature and pressure regime, and the layer never vanishes. The reported thickness influenced by the subcooling agrees with the previous work by Jiménez-Ángeles *et al*. at the established melting temperature of 287±1 K [91].

(a)

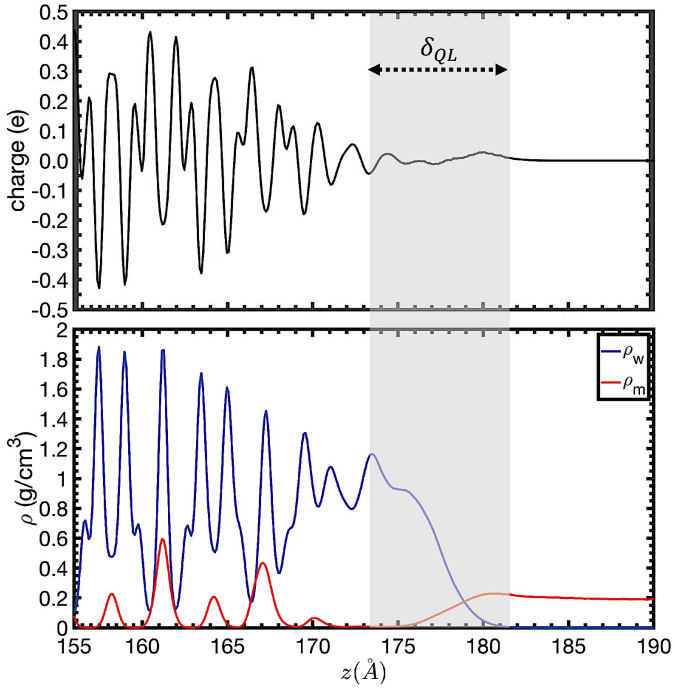


(b)

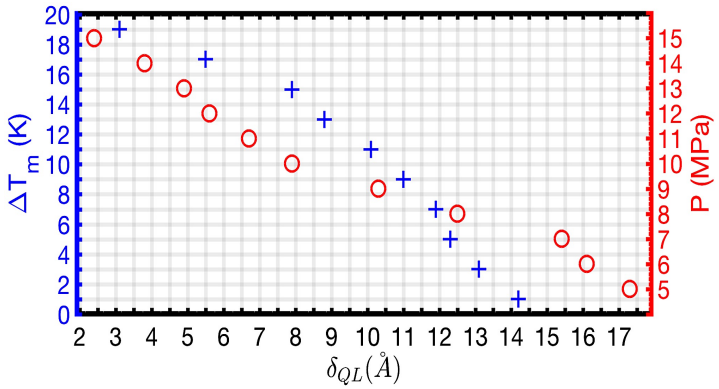


**Figure 6.** The plot (a) shows the charge and local density across the hydrate-gas interface at 275 K and 10 MPa to determine the quasi-liquid layer thickness. The blue and red lines represent the local density of water and methane molecules, respectively. The thickness of the intermediate quasi-liquid layer (b) formed between the methane gas and hydrate phases at different pressure (circle signs) and subcooling level (plus signs). The blue and red data are for the systems at constant 10 MPa and 275 K, respectively. This thickness decreases with pressure and subcooling.

Figure 7 shows the disjoining pressure of the methane hydrate and gas mixture at different temperature and pressure as per Eqn. (12). The imbalance between the attractive and repulsive forces of the broken bonds at the hydrate and gas interfaces causes a series of negative Π, which means these interfaces experience an increasingly attractive force when they approach each other. This disjoining pressure increases with temperature increase or pressure drop. We may insert the disjoining pressure and thickness data into the well-known Hamaker's formula [96] to obtain the Hamaker constant ($A$), and consequently, validate our results:

$$\Pi = -\frac{A}{6\pi {\delta_{QL}}^3} \tag{14}$$

The average Hamaker constant in this work is $3.11 \times 10^{-19}$ J, which is consistent with the value of $1.140 \times 10^{-19}$ J for methane hydrates in vacuum [97] or $3 \times 10^{-19}$ J [98] and $4 \times 10^{-19}$ J [99] obtained for similar water-metal mixtures conforming to the resemblance of crystalline structure of methane hydrates to metals.

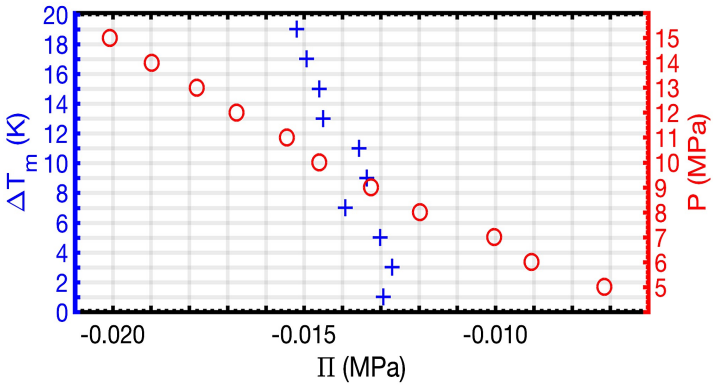


**Figure 7.** The disjoining pressure at different pressure (circle signs) and temperature (plus signs) regimes. The blue and red data are for the systems at constant 10 MPa and 275 K, respectively. High pressure or subcooling drops this pressure.

Depending on the definition of the spreading coefficient *S* and the material properties and structure in the interfacial region, the spreading coefficient might be zero, positive, or negative [100, 101]. We find that *S* is negative in the methane hydrate and gas mixture owing to the perpetual negative disjoining pressure at temperature and pressure ranges of 271-289 K and 5-15 MPa, respectively. Negative spreading coefficient is required for the premelting process at the interface [86].

In addition to Eqn. (13), the classical definition of the spreading coefficient is [94, 100, 102]:

$$S = \gamma_{hg} - \gamma_{hg}^{*} \tag{15}$$

This relation combined with the negative *S* implies that $\gamma_{hg}$ must always be lower than $\gamma_{hg}^{*}$. Hence, we conclude that the usage of the approximating Antonow's rule interfacial tension at the methane hydrate-gas interface suggested by Kashchiev *et al*. [19] yields inaccurate results because of the liquid-like film that forms on the interface. Please note that this conclusion is based on the negative spreading coefficient at the interface of sI methane hydrate-methane gas, while this layer can play a different role in a system with a different structure. Next, with the known interfacial tensions at the different interfaces, we proceed to calculate the work of cluster formation.

Figure 8 represents the formation work after numerical calculation for different nucleation scenarios of the pure methane hydrate at two sets of system temperature and pressure with a typical set of parameters, which are $c = \sqrt[3]{36\pi}$ for spherical clusters and $v_h$ = 0.216 nm$^3$ [19, 36]. The

lowest work belongs to a complete surface wetting that forms a film or disk-like interface as the interfacial energy does not intervene in this form of nucleation morphology. In addition to the effect of favorable thermodynamic regime (i.e., high pressure and low temperature), the cap-shaped cluster with more wetting surface (small $\theta$) lowers the work needed for formation of methane hydrates. We increase the formation work with the wetting angle until we utterly lose the wetting concept to reach the work equal to homogeneous nucleation scenario. Interfacial energy at different surfaces of lens-shaped nucleation controls the formation so that the morphology is analogous to the homogeneous case, which triggers similar formation work. For instance, the $\alpha$ and $\beta$ of the system at 275 K and 10 MPa are 151.61° and 9.99°, respectively. $\alpha+\beta=161.6°$ leads to a cluster submerged mostly in the water phase, rather than the gas phase. Not to mention that the lens-shaped nucleation is energetically more favorable compared to homogenous nucleation. Using Antonow's rule concludes the same work of formation for both lens-shaped and homogeneous forms [19], however the negative spreading parameter in the intermediate quasi-liquid layer between the gas and hydrate phases causes deviation from the Antonow's rule, which lowers the interfacial tension, and thus, the formation work. Hence, the premelting methane hydrate crystal at the hydrate-gas interface works in favor of the lens-shaped hydrate formation.

In conclusion, the methane solution theoretically tends to initiate nucleation in the ranked order of film-shaped, cap-shaped, lens-shaped, and lastly homogeneous. Nevertheless, the subtle difference between the formation work of homogeneous and lens-shaped configurations implies that the abundance of water and methane gas molecules at the interface of methane gas and liquid phases, not the interfacial energy contribution, is the main reason underlying higher thermodynamic probability of the lens-shaped nucleation, against homogeneous clustering, so that the labile hydrate clusters are adsorbed and agglomerated on the gas-liquid interface to form local structures of nucleation.

As discussed above, high supersaturation as the driving force of the cluster formation reduces its work. With hydrate crystal expansion, the interfacial energy contribution prevails over the supersaturation effect hindering the formation until the number of unit cells reaches the point that the energy role reversal occurs in the favor of formation by the driving force. Such critical number of crystal unit cells, corresponding to a critical radius of hydrate phase, and its maximum formation

work can be mathematically calculated by taking the first derivative of the expression for work of cluster formation with respect to *n*:

$$n^* = \frac{8c^3 v_h^2 \gamma^3}{27\Delta\mu^3} \tag{16}$$

$$W^* = \frac{4c^3 v_h^2 \gamma^3}{27\Delta\mu^2} \tag{17}$$

Figure 9 demonstrates that the lens-shaped or cap-shaped heterogeneous clustering with a small wetting angle are more favorable than homogeneous nucleation in order to physically reduce the energy barrier of formation. As per Eqn. (16) and (17), the $n^*$ and $W^*$ for the film-shaped case equal to zero, which lead to a formation process with no critical nucleus and induction period. While, this low energy cost theoretically supports the high possibility of hydrate film formation as previously shown [103, 104], we neglect this scenario in the calculation of critical size and work as it may obey a different set of formulations. Furthermore, Figure 10 summarizes how this formation barrier is minimized by the pressure and temperature, regarded as the most important thermodynamic conditions in hydrate crystal nucleation. In agreement with the experiments [1], low temperature and high pressure provide the perfect setting for the hydrate crystal nucleation to occur.

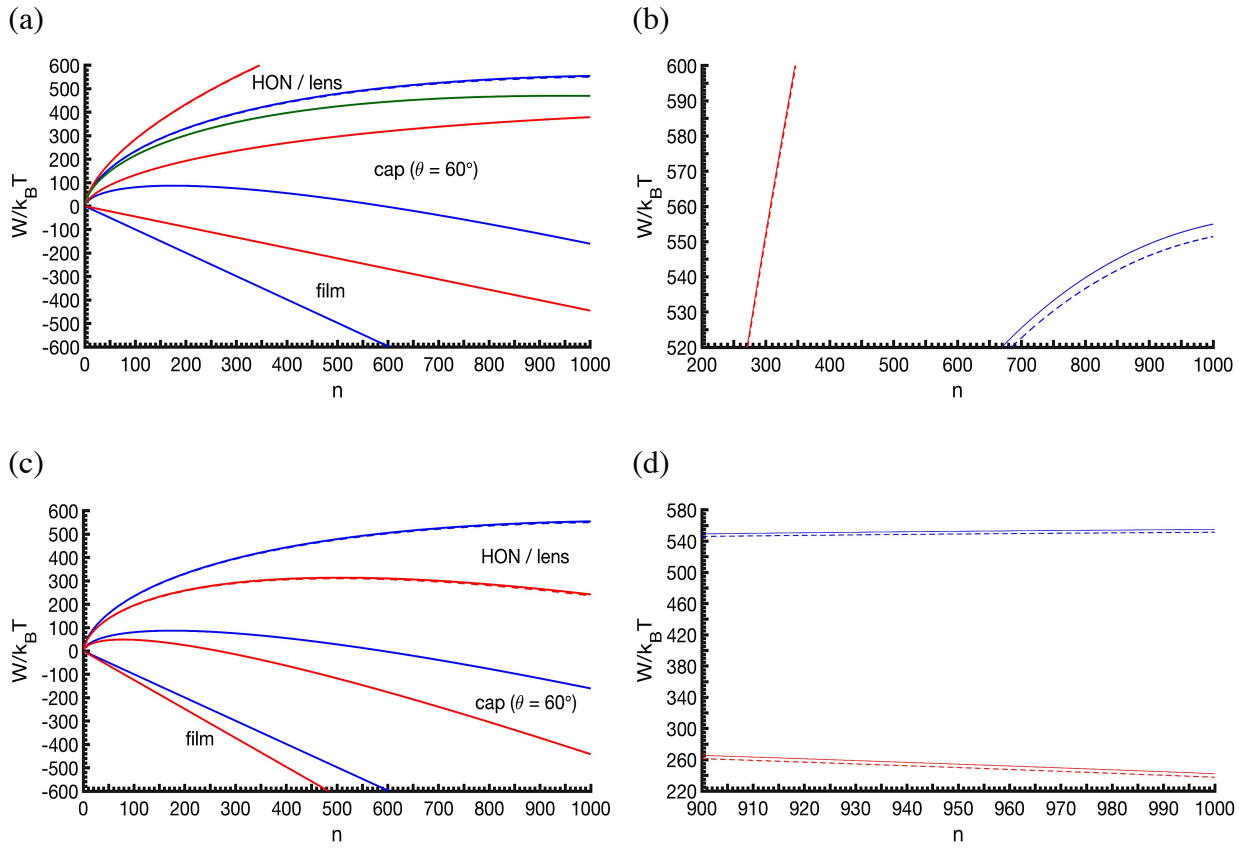


**Figure 8.** Work of methane hydrate nucleation under different formation scenarios and thermodynamic conditions. The plot (a) is for a system at 275 K (blue line) and 281 K (red line) with the constant pressure of 10 MPa. The green line shows the work for the cap-shaped clustering with $\theta$ of 120°. The formation work increases as the system temperature increases. The film-shaped, cap-shaped, and lens-shaped nucleation lower the work of formation compared to the homogeneous case. The plot (b) distinguishes the difference between homogeneous (solid) and lens-shape (dashed) nucleation work. The plot (c) is for a system at 10 MPa (blue line) and 15 MPa (red line) with the constant temperature of 275 K. The work of formation decreases with pressure. The plot (d) magnifies the variation between the work of lens-shape (dashed) and homogeneous (solid) formation.

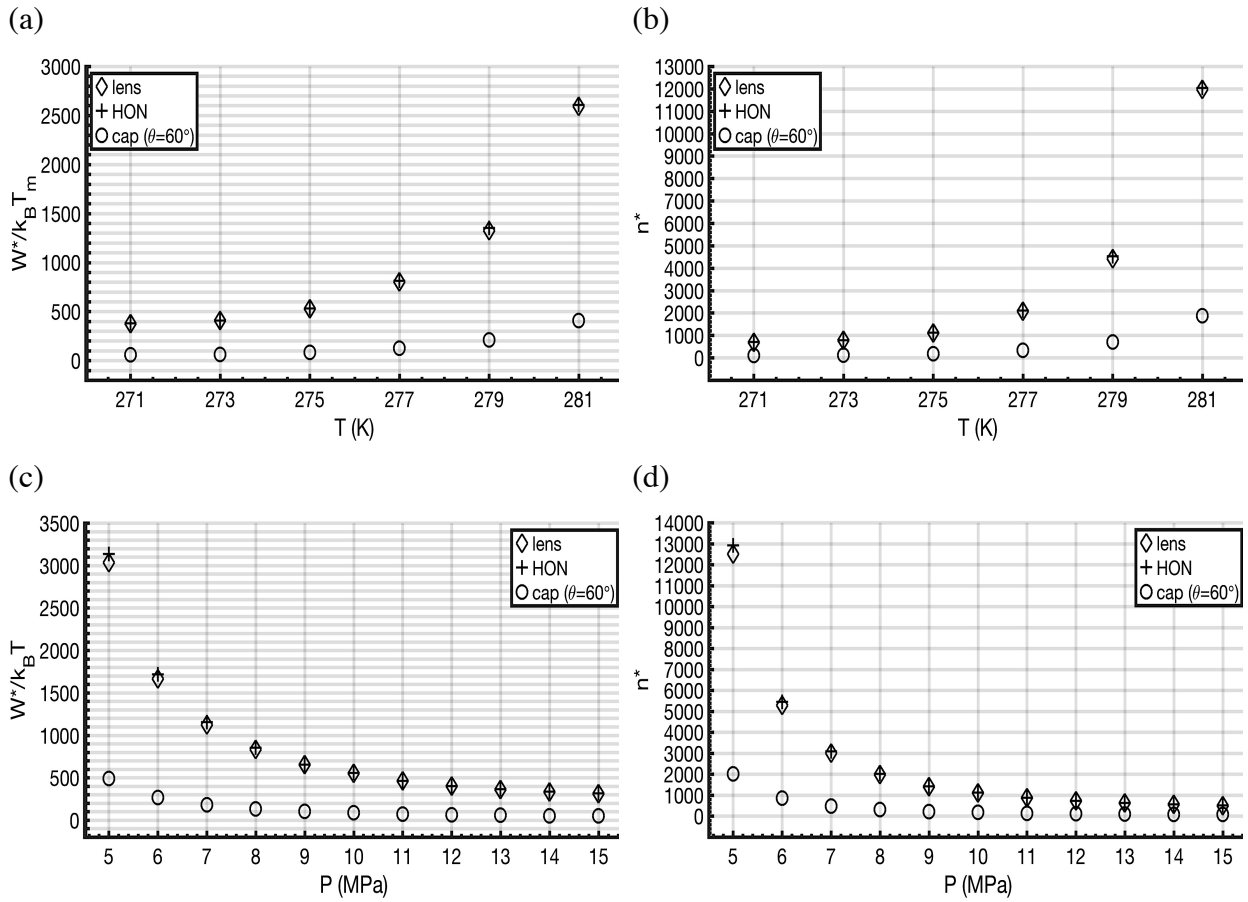


**Figure 9.** Maximum formation work and its corresponding number of crystal unit cells depend on the cluster formation shape (homogenous or heterogeneous), temperature (a and b) at 10 MPa, and pressure (c and d) at 275 K. The system with high pressure, low temperature, and heterogeneous clustering with a small wetting angle requires lower work of formation. Furthermore, lens-shaped heterogeneous formation is narrowly favorable compared to the homogeneous nucleation.

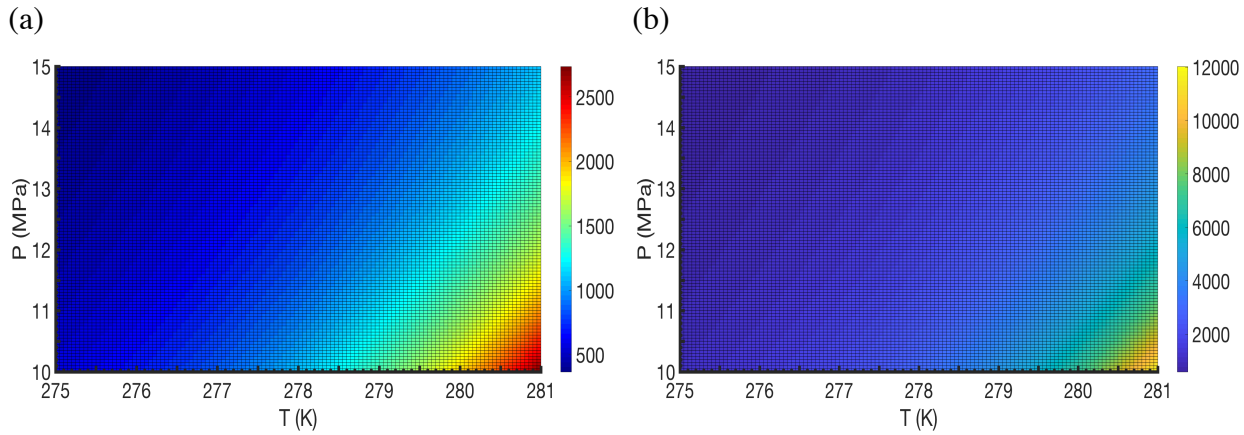


**Figure 10.** The maximum formation work in units of $k_BT$ (a) and critical number of crystal unit cells (b) for homogeneous nucleation at different pressure and temperature. Low temperature and high-pressure thermodynamic conditions require minimum formation work and critical size, which vastly facilitate the hydrate nucleation process.

Next, we determine the rate of hydrate cluster formation in order to study the effect of the involved surfaces in the crystal nucleation rate. We consider the general expression in single-component gas hydrate system [19]. Hence, the nucleation rate ($J$) in units of $1/m^3s$ can be obtained from:

$$J = Aexp\left(\frac{\Delta\mu}{k_BT} - \frac{4c^3v_h^2\gamma^3}{27k_BT\Delta\mu^2}\right) \tag{18}$$

where $A$ ($1/m^3s$) is the kinetic factor that accounts for the attachment mechanism of the crystal unit cells to the cluster depending on the nucleation type (HON or HEN). This factor is independent of the supersaturation condition. In addition, we include additives in the solution obeying the Langmuir adsorption isotherm to evaluate the covering effect on the cluster active surface (i.e., the involved surface in the formation process). Please note that the impact of additives on the surface energy is not the concern of this work. Therefore, the nucleation rate of hydrate clusters with a fraction of the active surface is calculated by the expression below:

$$J = \left(\frac{A}{1+k_nC_a}\right) exp\left(\frac{\Delta\mu - W^*}{k_BT}\right) \tag{19}$$

where $k_n$ ($m^3$) and $C_a$ ($1/m^3$) are the Langmuir adsorption constant and the additive concentration, respectively. Please note that we choose $k_n$ so that the additive adsorption is assumed to be independent of the system temperature and pressure. Figure 11 depicts how the nucleation

morphology and the additive concentration contribute in the crystalline nucleation rate. The reported trend and magnitude of nucleation rates are consistent with previous experimental analysis performed for methane hydrates [105]. All heterogeneous nucleation forms including film, cap, and lens shapes expectedly increase the nucleation rate in different pressure and temperature regimes. According to these nucleation rate results, the ranked order of nucleation shapes reconciles with the results obtained from the formation work.

Herein, one may inhibit the hydrate formation with supplying an additive in the solution provided that the additives are strongly adsorbed on the surface of the hydrate cluster, and do not generate new nucleation sites. High concentration of the surface covering additives might be used as kinetic inhibitor to solve the issue of pipeline blockage in petroleum industry. This current work on additives merely reveals the inhibiting effect due to the applied assumptions, while some additives promote the nucleation rate. Hence, there needs to be more focus on the significance of the additives on the surface energy, creation of new nucleation sites, and the attachment strength to mimic a more realistic model.

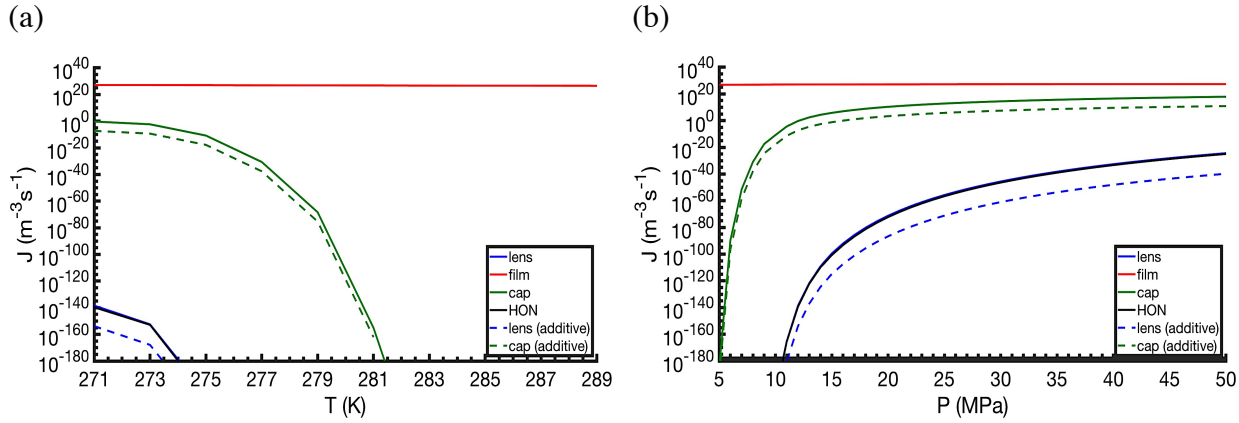


**Figure 11.** Gas hydrate nucleation rate in different temperature (a) and pressure (b) regimes with (dashed) or without (solid) additives. The constant pressure of plot (a) and temperature of plot (b) are 10 MPa and 275 K, respectively. $A$ is assumed to be $10^{35}$ and $4 \times 10^{26}$ 1/m$^3$s for HON and HEN nucleation processes, respectively [19]. Blue, red, green, and black lines represent the lens-shaped, film-shaped, cap-shaped, and homogeneous forms of clustering, respectively. In this work, we adopt the arbitrary values of $10^{-18}$ m$^3$ and $10^{25}$ 1/m$^3$ for $k_n$ and $C_a$, respectively.

Finally, we apply the ice-water interfacial tension of 29.1 mN/m [106] as a substitute to the hydrate-water interfacial tension for a system at 275 K and different pressures. Figure 12 clearly

shows that a slight change in such interfacial tension escalates the formation nucleation rate by orders of magnitude. Therefore, we inevitably need to use the interfacial tension values of methane hydrate to obtain the most sensible results.

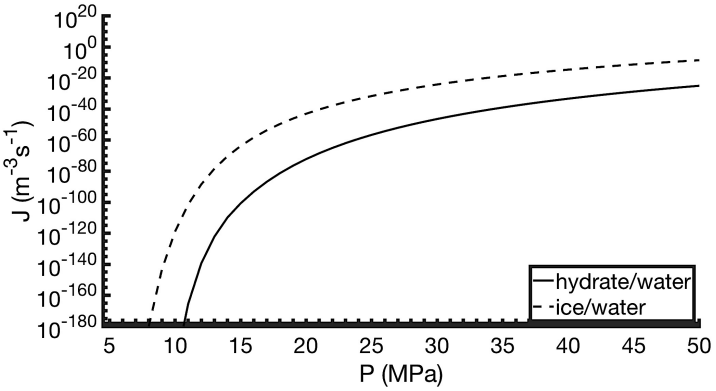


**Figure 12.** The formation nucleation rate using the interfacial tension of methane hydrate-water (solid line) and ice-water (dashed line) at 275 K. The rate is prodigiously higher when the ice-water properties are applied.

**Summary and Conclusions**

The interaction of methane gas and water at low temperature and high pressure may cause methane hydrate formation. In both industrial and natural environments, the nucleation appears in the solution bulk or at the solid-liquid and liquid-gas interfaces forming different morphologies. To promote or inhibit this nucleation process, we are able to further understand the work, location, and morphology of the formation through classical nucleation theory. Therefore, we employed a combination of molecular dynamics technique and theoretical computation to obtain the formation work. The main focus is on the interfacial energy contribution in the nucleation process of methane gas hydrates that has not been well studied before, while, it has shown a big effect in the widespread applications of clathrate hydrates, specifically in flow assurance owing to the chemical composition of natural gas.

We first computed the interfacial tension at water-methane hydrate and water-methane gas interfaces, and afterwards, applied our method and Antonow's rule to find the interfacial tension at the interface between methane hydrate and the gas phase. We showed that a quasi-liquid layer

was formed between the hydrate and gas phases due to the premelting process of crystalline hydrate in contact with the methane gas molecules. The existence of this thin intermediate layer causes the Antonow's rule to overestimate the interfacial tension, and consequently it cannot be used to estimate the tension values at the hydrate-gas interface, which was proposed by Kashchiev *et al*. [19]. With the necessary interfacial properties at hand we then calculated the formation work and nucleation rate of methane hydrate. We concluded that the nucleation was more favorable in low temperature and high pressure regimes, and likewise, at the water-methane hydrate interface in a shape of a film or disk. The other formation morphologies in order of likely occurrence were cap-shaped, lens-shaped, and homogeneous forms of nucleation, respectively. We proposed that the existence of a quasi-liquid layer between the methane hydrate and gas surfaces causes lower formation work for the lens-shaped formation compared to homogeneous. Nonetheless, high concentration of methane gas and water molecules at the surface, not the interfacial energy contribution as pointed by Aman *et al*. [20], is found to be the leading reason of lens-shape formation as opposed to homogeneous. In addition, we demonstrated that the presence of additives in the mixture of water-methane gas reduces the nucleation rate, which inhibited the hydrate formation process. Lastly, we presented the nucleation rate employing the interfacial tension at the ice surfaces, instead of hydrate, which led to significantly larger nucleation rates. This large discrepancy prevents the usage of ice properties from estimating the interfacial energy in hydrate studies.

In summary, the reported results on different aspects of methane hydrate critically deliver a qualitative and quantitative set of information in gas hydrate formation through the characterization of the water-hydrate, water-gas, and hydrate-gas interfaces. We anticipate this work will significantly contribute to a better understanding of the kinetics of clathrate hydrate formation in different thermodynamic pressure and temperature regimes and to the many technological processes that rely on interfacial science. However, other possible morphologies of methane hydrate nucleation such as sII methane hydrate may lead to distinct interfacial structures and shape factors, and consequently, alter the conclusions of this work. Moreover, a deeper analysis on the impact of surface covering additives on the surface energy, the attachment strength, and creation of new nucleation sites is necessary for surfactants applications. In addition to the study on the interfacial energy contribution, their needs to be more work performed on the

modeling of methane hydrate formation through the classical nucleation theory in regards to the supersaturation contribution into the nucleation process.

**Acknowledgements**

This research is financially supported by the McGill Engineering Doctoral Awards (MEDA), the James McGill Professorship appointment (ADR), and the Natural Sciences and Engineering Research Council (NSERC). The authors are also grateful to Compute Canada and Calcul Québec for the access to the supercomputers Graham and Cedar, and their technical assistance.

**References**

1. Sloan Jr, E.D. and C. Koh, *Clathrate hydrates of natural gases*. 2007: CRC press.
2. Jendi, Z.M., P. Servio, and A.D. Rey, *Ideal strength of methane hydrate and ice Ih from first-principles*. Crystal Growth & Design, 2015. **15**(11): p. 5301-5309.
3. Vlasic, T.M., P. Servio, and A.D. Rey, *Atomistic modeling of structure II gas hydrate mechanics: Compressibility and equations of state*. AIP Advances, 2016. **6**(8): p. 085317.
4. Vlasic, T.M., P.D. Servio, and A.D. Rey, *Effect of guest size on the mechanical properties and molecular structure of gas hydrates from first-principles*. Crystal Growth & Design, 2017. **17**(12): p. 6407-6416.
5. Carroll, J., *Natural gas hydrates: a guide for engineers*. 2014: Gulf Professional Publishing.
6. Ginley, D.S. and D. Kahen, *Fundamentals of materials for energy and environmental sustainability*. 2012, Cambridge; New York: Cambridge University Press.
7. Riedel, M., E.C. Willoughby, and S. Chopra, *Geophysical characterization of gas hydrates*. 2010, Tulsa, OK: Society of Exploration Geophysicists.
8. Koh, C.A., et al., *Fundamentals and applications of gas hydrates*. 2011.
9. Englezos, P. and J.D. Lee, *Gas hydrates: A cleaner source of energy and opportunity for innovative technologies*. Korean Journal of Chemical Engineering, 2005. **22**(5): p. 671-681.
10. Klauda, J.B. and S.I. Sandler, *Global distribution of methane hydrate in ocean sediment*. Energy & Fuels, 2005. **19**(2): p. 459-470.
11. Demirbas, A., *Methane gas hydrate*. 2010: Springer Science & Business Media.
12. Sloan, E.D., *Fundamental principles and applications of natural gas hydrates*. Nature, 2003. **426**(6964): p. 353-363.
13. Fandiño, O. and L. Ruffine, *Methane hydrate nucleation and growth from the bulk phase: Further insights into their mechanisms*. Fuel, 2014. **117, Part A**: p. 442-449.
14. Sloan, E.D., *Natural gas hydrates in flow assurance*. 2011.
15. Zerpa, L.E., et al., *Surface chemistry and gas hydrates in flow assurance*. Industrial & Engineering Chemistry Research, 2011. **50**(1): p. 188-197.

16. Bai, X.-M. and M. Li, *Test of classical nucleation theory via molecular-dynamics simulation*. The Journal of chemical physics, 2005. **122**(22): p. 224510.
17. Lupi, L., B. Peters, and V. Molinero, *Pre-ordering of interfacial water in the pathway of heterogeneous ice nucleation does not lead to a two-step crystallization mechanism*. The Journal of chemical physics, 2016. **145**(21): p. 211910.
18. Warrier, P., et al., *Overview: Nucleation of clathrate hydrates*. The Journal of chemical physics, 2016. **145**(21): p. 211705.
19. Kashchiev, D. and A. Firoozabadi, *Nucleation of gas hydrates*. Journal of Crystal Growth, 2002. **243**(3–4): p. 476-489.
20. Aman, Z.M. and C.A. Koh, *Interfacial phenomena in gas hydrate systems*. Chemical Society Reviews, 2016. **45**(6): p. 1678-1690.
21. Tanaka, R., R. Sakemoto, and R. Ohmura, *Crystal growth of clathrate hydrates formed at the interface of liquid water and gaseous methane, ethane, or propane: variations in crystal morphology*. Crystal Growth & Design, 2009. **9**(5): p. 2529-2536.
22. Asserson, R.B., et al., *Interfacial tension measurement of freon hydrates by droplet deposition and contact angle measurements*. Journal of Petroleum Science and Engineering, 2009. **68**(3–4): p. 209-217.
23. Sun, C.Y., et al., *Studies on hydrate film growth*. Annual Reports Section "C" (Physical Chemistry), 2010. **106**(0): p. 77-100.
24. Koop, T. and B.J. Murray, *A physically constrained classical description of the homogeneous nucleation of ice in water*. The Journal of chemical physics, 2016. **145**(21): p. 211915.
25. Sarupria, S. and P.G. Debenedetti, *Homogeneous nucleation of methane hydrate in microsecond molecular dynamics simulations*. The journal of physical chemistry letters, 2012. **3**(20): p. 2942-2947.
26. Knott, B.C., et al., *Homogeneous nucleation of methane hydrates: Unrealistic under realistic conditions*. Journal of the American Chemical Society, 2012. **134**(48): p. 19544-19547.
27. Bagherzadeh, S.A., et al., *Influence of hydrated silica surfaces on interfacial water in the presence of clathrate hydrate forming gases*. The Journal of Physical Chemistry C, 2012. **116**(47): p. 24907-24915.
28. Bai, D., et al., *How properties of solid surfaces modulate the nucleation of gas hydrate*. Scientific Reports, 2015. **5**: p. 12747.
29. Liang, S. and P.G. Kusalik, *The nucleation of gas hydrates near silica surfaces*. Canadian Journal of Chemistry, 2014. **93**(8): p. 791-798.
30. Koga, T., et al., *Hydrate formation at the methane/water interface on the molecular scale*. Langmuir, 2010. **26**(7): p. 4627-4630.
31. Zhao, J., et al., *Microstructural characteristics of natural gas hydrates hosted in various sand sediments*. Physical Chemistry Chemical Physics, 2015. **17**(35): p. 22632-22641.
32. Davies, S.R., et al., *Studies of hydrate nucleation with high pressure differential scanning calorimetry*. Chemical Engineering Science, 2009. **64**(2): p. 370-375.
33. Englezos, P., et al., *Kinetics of formation of methane and ethane gas hydrates*. Chemical Engineering Science, 1987. **42**(11): p. 2647-2658.
34. Vatamanu, J. and P.G. Kusalik, *Observation of two-step nucleation in methane hydrates*. Physical Chemistry Chemical Physics, 2010. **12**(45): p. 15065-15072.

35. Zhang, Z. and G.-J. Guo, *The effects of ice on methane hydrate nucleation: a microcanonical molecular dynamics study*. Physical Chemistry Chemical Physics, 2017. **19**(29): p. 19496-19505.
36. Kashchiev, D. and A. Firoozabadi, *Driving force for crystallization of gas hydrates*. Journal of Crystal Growth, 2002. **241**(1–2): p. 220-230.
37. Kashchiev, D. and A. Firoozabadi, *Induction time in crystallization of gas hydrates*. Journal of crystal growth, 2003. **250**(3-4): p. 499-515.
38. Khadem, S.A. and A.D. Rey, *Thermodynamic modelling of acidic collagenous solutions: from free energy contributions to phase diagrams*. Soft matter, 2019. **15**(8): p. 1833-1846.
39. Kashchiev, D., *Nucleation : basic theory with applications*. 2000, Butterworth Heinemann: Oxford ;.
40. Khadem, S.A. and R.B. Boozarjomehry, *Development of systematic framework for an intelligent decision support system in gas transmission network*. Industrial & Engineering Chemistry Research, 2015. **54**(43): p. 10768-10786.
41. Khadem, S.A., et al., *Pressure and temperature functionality of paraffin-carbon dioxide interfacial tension using genetic programming and dimension analysis (GPDA) method*. Journal of Natural Gas Science and Engineering, 2014. **20**: p. 407-413.
42. Khadem, S.A. and A. Rey, *Theoretical Platform for Liquid-Crystalline Self-assembly of Collagen-Based Biomaterials*. Frontiers in Physics, 2019. **7**: p. 88.
43. Binks, B.P. and J.H. Clint, *Solid wettability from surface energy components: relevance to pickering emulsions*. Langmuir, 2002. **18**(4): p. 1270-1273.
44. Vázquez, U.O.M., et al., *Calculating the surface tension between a flat solid and a liquid: a theoretical and computer simulation study of three topologically different methods*. Journal of Mathematical Chemistry, 2009. **45**(1): p. 161-174.
45. Chaplin, M., *Theory vs experiment: what is the surface charge of water?* Water Journal Multidisciplinary Research Journal 1, 2009: p. 1-28.
46. Eisenberg, D., D.S. Eisenberg, and W. Kauzmann, *The structure and properties of water*. 2005: Oxford University Press on Demand.
47. Kirkwood, J.G. and F.P. Buff, *The statistical mechanical theory of surface tension*. The Journal of Chemical Physics, 1949. **17**(3): p. 338-343.
48. Tolman, R.C., *Consideration of the Gibbs theory of surface tension*. The journal of chemical physics, 1948. **16**(8): p. 758-774.
49. Takeuchi, F., et al., *Water proton configurations in structures I, II, and H clathrate hydrate unit cells*. The Journal of chemical physics, 2013. **138**(12): p. 124504.
50. Gutt, C., et al., *The structure of deuterated methane–hydrate*. The journal of chemical physics, 2000. **113**(11): p. 4713-4721.
51. Conde, M. and C. Vega, *Determining the three-phase coexistence line in methane hydrates using computer simulations*. The Journal of chemical physics, 2010. **133**(6): p. 064507.
52. Soustelle, M., *Thermodynamics of surfaces and capillary systems*. 2016, ISTE, Ltd. ; John Wiley & Sons: London, UK; Hoboken, NJ.
53. Erbil, H.Y., *Surface chemistry of solid and liquid interfaces*. 2006, Oxford, UK ;: Blackwell Pub.

54. Jorgensen, W.L., J.D. Madura, and C.J. Swenson, *Optimized intermolecular potential functions for liquid hydrocarbons*. Journal of the American Chemical Society, 1984. **106**(22): p. 6638-6646.
55. Horn, H.W., et al., *Development of an improved four-site water model for biomolecular simulations: TIP4P-Ew*. The Journal of chemical physics, 2004. **120**(20): p. 9665-9678.
56. Plimpton, S., *Fast parallel algorithms for short-range molecular dynamics*. Journal of computational physics, 1995. **117**(1): p. 1-19.
57. Krouskop, P.E., et al., *Solubility of simple, nonpolar compounds in TIP4P-Ew*. The Journal of chemical physics, 2006. **124**(1): p. 016102.
58. Tung, Y.-T., et al., *The growth of structure I methane hydrate from molecular dynamics simulations*. The Journal of Physical Chemistry B, 2010. **114**(33): p. 10804-10813.
59. Zielkiewicz, J., *Structural properties of water: Comparison of the SPC, SPCE, TIP4P, and TIP5P models of water*. The Journal of chemical physics, 2005. **123**(10): p. 104501.
60. Hockney, R.W. and J.W. Eastwood, *Computer simulation using particles*. 1988: crc Press.
61. Isele-Holder, R.E., W. Mitchell, and A.E. Ismail, *Development and application of a particle-particle particle-mesh Ewald method for dispersion interactions*. The Journal of chemical physics, 2012. **137**(17): p. 174107.
62. Mirzaeifard, S., P. Servio, and A.D. Rey, *Multiscale Modeling and Simulation of Water and Methane Hydrate Crystal Interface*. Crystal Growth & Design, 2019.
63. Firoozabadi, A., *Thermodynamics of hydrocarbon reservoirs*. 1999: McGraw-Hill.
64. Ghiass, M. and A.D. Rey, *Interfacial thermodynamics of compressible polymer solutions*. 2008, AIP.
65. Rowlinson, J.S. and B. Widom, *Molecular theory of capillarity*. 2013: Courier Corporation.
66. Blokhuis, E., et al., *Tail corrections to the surface tension of a Lennard-Jones liquid-vapour interface*. Molecular Physics, 1995. **85**(3): p. 665-669.
67. Chapela, G.A., et al., *Computer simulation of a gas–liquid surface. Part 1*. Journal of the Chemical Society, Faraday Transactions 2: Molecular and Chemical Physics, 1977. **73**(7): p. 1133-1144.
68. Grest, G.S., et al., *Substructured multibody molecular dynamics*. 2006, Sandia National Laboratories.
69. Qi, X., T. Balankura, and K.A. Fichthorn, *Theoretical Perspectives on the Influence of Solution-Phase Additives in Shape-Controlled Nanocrystal Synthesis*. The Journal of Physical Chemistry C, 2018. **122**(33): p. 18785-18794.
70. Mirzaeifard, S., P. Servio, and A.D. Rey, *Molecular Dynamics Characterization of the Water-Methane, Ethane, and Propane Gas Mixture Interfaces*. Chemical Engineering Science, 2019.
71. Mirzaeifard, S., P. Servio, and A.D. Rey, *Molecular dynamics characterization of temperature and pressure effects on the water-methane interface*. Colloid and Interface Science Communications, 2018. **24**: p. 75-81.
72. Høiland, S., et al. *Wettability of Freon hydrates in crude oil/brine emulsions: The effect of chemical additives*. in *Proceedings of the 5th International Conference on Gas Hydrates*. 2005.
73. Peeters, P., *Nucleation and condensation in gas-vapor mixtures of alkanes and water*. 2004.

74. Aman, Z.M., et al., *Surfactant adsorption and interfacial tension investigations on cyclopentane hydrate*. Langmuir, 2013. **29**(8): p. 2676-2682.
75. Hu, S. and C.A. Koh, *Interfacial properties and mechanisms dominating gas hydrate cohesion and adhesion in liquid and vapor hydrocarbon phases*. Langmuir, 2017. **33**(42): p. 11299-11309.
76. Naeiji, P., F. Varaminian, and M. Rahmati, *Comparison of the thermodynamic, structural and dynamical properties of methane/water and methane/water/hydrate systems using molecular dynamic simulations*. Journal of Natural Gas Science and Engineering, 2017. **44**: p. 122-130.
77. Kvamme, B., T. Kuznetsova, and K. Schmidt. *Experimental measurements and numerical modelling of interfacial tension in water-methane systems*. in *Presentation at the International Conference of Computational Methods in Sciences and Engineering, Chania, Greece*. 2006.
78. Schmidt, K.A., G.K. Folas, and B. Kvamme, *Calculation of the interfacial tension of the methane–water system with the linear gradient theory*. Fluid Phase Equilibria, 2007. **261**(1): p. 230-237.
79. Jho, C., et al., *Effect of pressure on the surface tension of water: Adsorption of hydrocarbon gases and carbon dioxide on water at temperatures between 0 and 50 C*. Journal of Colloid and Interface Science, 1978. **65**(1): p. 141-154.
80. Jacobson, L.C. and V. Molinero, *Can amorphous nuclei grow crystalline clathrates? The size and crystallinity of critical clathrate nuclei*. Journal of the American Chemical Society, 2011. **133**(16): p. 6458-6463.
81. Anderson, R., et al., *Experimental measurement of methane and carbon dioxide clathrate hydrate equilibria in mesoporous silica*. The Journal of Physical Chemistry B, 2003. **107**(15): p. 3507-3514.
82. Uchida, T., et al., *Effects of pore sizes on dissociation temperatures and pressures of methane, carbon dioxide, and propane hydrates in porous media*. The journal of physical chemistry B, 2002. **106**(4): p. 820-826.
83. Djikaev, Y. and E. Ruckenstein, *Self-Consistent Determination of the Ice–Air Interfacial Tension and Ice–Water–Air Line Tension from Experiments on the Freezing of Water Droplets*. The Journal of Physical Chemistry C, 2017. **121**(30): p. 16432-16439.
84. Djikaev, Y.S. and E. Ruckenstein, *Dependence of homogeneous crystal nucleation in water droplets on their radii and its implication for modeling the formation of ice particles in cirrus clouds*. Physical Chemistry Chemical Physics, 2017. **19**(30): p. 20075-20081.
85. Dufour, L. and R. Defay, *Thermodynamics of clouds*. International geophysics series ; v. 6. 1963, New York: Academic Press.
86. Dash, J., A. Rempel, and J. Wettlaufer, *The physics of premelted ice and its geophysical consequences*. Reviews of modern physics, 2006. **78**(3): p. 695.
87. Wettlaufer, J., *Impurity effects in the premelting of ice*. Physical Review Letters, 1999. **82**(12): p. 2516.
88. Döppenschmidt, A. and H.-J. Butt, *Measuring the thickness of the liquid-like layer on ice surfaces with atomic force microscopy*. Langmuir, 2000. **16**(16): p. 6709-6714.
89. Maruyama, M., et al., *Interfacial melting of ice in graphite and talc powders*. Journal of crystal growth, 1992. **118**(1-2): p. 33-40.

90. Shepherd, T.D., M.A. Koc, and V. Molinero, *The quasi-liquid layer of ice under conditions of methane clathrate formation*. The Journal of Physical Chemistry C, 2012. **116**(22): p. 12172-12180.
91. Jiménez-Ángeles, F. and A. Firoozabadi, *Induced charge density and thin liquid film at hydrate/methane gas interfaces*. The Journal of Physical Chemistry C, 2014. **118**(45): p. 26041-26048.
92. Sedev, R., *Fundamentals of Surface Forces*. 2014.
93. Rey, A.D., *Mechanical theory of structural disjoining pressure in liquid crystal films*. Physical Review E, 2000. **61**(4): p. 4632.
94. Rey, A.D., *Mechanical theory for nematic thin films*. Langmuir, 2001. **17**(6): p. 1922-1927.
95. Emelyanenko, K., A. Emelyanenko, and L. Boinovich, *Spreading and contraction of a benzene lens on water: A description on the basis of the disjoining pressure*. Colloids and Surfaces A: Physicochemical and Engineering Aspects, 2017. **522**: p. 601-607.
96. Hamaker, H.C., *The London—van der Waals attraction between spherical particles*. physica, 1937. **4**(10): p. 1058-1072.
97. Bonnefoy, O., F. Gruy, and J.-M. Herri, *Van der Waals interactions in systems involving gas hydrates*. Fluid Phase Equilibria, 2005. **231**(2): p. 176-187.
98. Hu, H. and Y. Sun, *Molecular dynamics simulations of disjoining pressure effect in ultra-thin water film on a metal surface*. Applied Physics Letters, 2013. **103**(26): p. 263110.
99. Parsegian, V.A. and G.H. Weiss, *Spectroscopic parameters for computation of van der Waals forces*. Journal of Colloid and Interface Science, 1981. **81**(1): p. 285-289.
100. De Gennes, P.-G., *Wetting: statics and dynamics*. Reviews of modern physics, 1985. **57**(3): p. 827.
101. Sadiki, M., et al., *Adsorption and wetting mechanisms at the surface of aqueous hydrocarbon solutions as a possible source of atmospheric pollution*. Oil & Gas Science and Technology-Revue de l'IFP, 2006. **61**(5): p. 661-676.
102. Loret, B., *Fluid Injection in Deformable Geological Formations: Energy Related Issues*. 2018: Springer.
103. Li, S.-L., et al., *New observations and insights into the morphology and growth kinetics of hydrate films*. Scientific reports, 2014. **4**: p. 4129.
104. Sun, C., et al., *Studies on hydrate film growth*. Annual Reports Section" C"(Physical Chemistry), 2010. **106**: p. 77-100.
105. Thoutam, P., et al., *Comparative Analysis of Hydrate Nucleation for Methane and Carbon Dioxide*. Molecules, 2019. **24**(6): p. 1055.
106. Hardy, S., *A grain boundary groove measurement of the surface tension between ice and water*. Philosophical Magazine, 1977. **35**(2): p. 471-484.